

Cold spray deposition for additive manufacturing of freeform structural components compared to selective laser melting

Sara Bagherifard^a, Stefano Monti^a, Maria Vittoria Zuccoli^a, Martina Riccio^b, Ján Kondás^c, Mario Guagliano^{a,*}

^a Politecnico di Milano, Department of Mechanical Engineering, Via La Masa 1, 20156 Milan, Italy

^b Beam-IT Spa, Strada Prinzer, 17, 43045 Fornovo di Taro PR, Italy

^c Impact Innovations GmbH, Bürgermeister-Steinberger-Ring 1, 84431 Haun/Rattenkirchen, Germany

ARTICLE INFO

Keywords:

Additive manufacturing
Cold spray
Selective laser melting (SLM)
Inconel 718
Fatigue strength

ABSTRACT

Recent advances in the field of cold spray have put forward the potential of this deposition technique to be used as a non-thermal additive manufacturing process with significantly high deposition rates. In this study, we use the additive manufacturing potential of cold spray for fabrication of freestanding three-dimensional Inconel 718 samples, which is a challenging material for cold spray due to its high hardness and limited deformability. Additionally, we fabricated samples with similar geometry using one of the most common additive manufacturing methods, i.e. selective laser melting. Microstructural characteristics, distribution of residual stresses, porosity and structural integrity of the cold spray deposited samples were compared with those obtained by selective laser melting before and after different heat treatments. The results of the first time study of axial fatigue strength of cold spray deposited freeform samples indicate the notable efficiency of cold spray for fabrication of freestanding objects for structural components, with similar characteristics to those obtained from laser based additive manufacturing technique and even comparable to bulk material properties. The low working temperature of the cold spray method, suggests it as a promising additive manufacturing technique with a high potential to address many challenges regarding laser based approaches.

1. Introduction

Cold spray (CS) is an emerging non-thermal deposition method with exciting applications coming along every day. In CS, bonding takes place when the velocity of the particles, that are accelerated by high pressure and pre-heated supersonic gas stream exceed a critical velocity [1]. The intrinsic features of CS are the possibility of depositing metallic powders at solid state at working temperatures much lower than the melting point of any of the involved materials [2,3]. Thus, the main basis of bonding in CS is kinetic energy, contrary to other thermal spray coating techniques that rely on thermal energy to induce metallurgical bonding. Thus far, CS has been mostly used as a mass production coating technique for thick coating deposition, corrosion protection or dimensional restoration and repair [3,4]. However, the possibility of obtaining highly dense deposits with no theoretical limit to the thickness brings on the most recent application in the horizon for CS that is additive manufacturing (AM). CS process can offer numerous advantages in the field of AM compared to other common powder bed layer by layer fabrication techniques including selective laser melting/

sintering (SLM/SLS), direct metal deposition (DMD) and electron beam melting (EBM). Such advantages can be listed as:

- i) the opportunity to be used for deposition of temperature/oxygen sensitive material since no extra heat comes into play contrary to laser based AM techniques [5];
- ii) induction of minimal or compressive residual stresses contrary to tensile residual stresses typically induced in laser based AM techniques;
- iii) the prospect of obtaining a wide range of multimaterial and/or functionally graded deposits, whereas laser based methods are limited by different thermal conductivity and expansion characteristics of dissimilar powder types;
- iv) notably high deposition rates of CS (300–400 cm³/h [6] and in some cases up to 1500 cm³/h), which make it a fairly scalable AM technology;
- v) less dimensional restrictions compared to the laser based AM techniques with limited working area under controlled environment (vacuum/inert gas).

* Corresponding author.

E-mail address: mario.guagliano@polimi.it (M. Guagliano).

SLM is an additive manufacturing technology that allows layer by layer building of metallic components using laser source to fuse the melted powder particles together. It has received significant attention in the recent years for the multiple advantages it can offer compared to conventional manufacturing technologies [7] and has been widely used for near net shape fabrication of parts from various alloys and composite materials with outstanding mechanical performance [8–10]. The major advantage of laser based AM methods over CS is the significant geometrical accuracy, which can define the precision of the final product compared to the relatively low spatial resolution of CS (hundreds of micron vs. few mm) [11]. In SLM technique, quite fine spot size, mainly defined by laser beam diameter and the powder size, provide the possibility of obtaining highly intricate customized shapes; while in CS, the nozzle shape and geometry are the main defining parameters that provide less precision on the spray feature size with the current technology [12]. The target area for freestanding objects deposited by CS, are mainly large scale deposits with near net shape accuracy, which are not feasible by conventional powder bed AM techniques. Besides, the research performed on the potential of CS to be used for fabrication of freeform objects shows adequate machinability by standard milling and turning techniques for CS near net-shape deposits [12].

There are few recent interesting studies about the application of CS technology as an AM technique mainly for fabrication of Nickel–aluminum [13], pure aluminum [14–16], Zinc [17] and Ti alloys [6,18]. Nevertheless, there are still very limited data on microstructural and mechanical characteristics of CS deposited freestanding objects. In addition, CS deposits have been traditionally used for non-structural applications. As the future of CS technology is moving towards fabrication of load bearing structural components, it of utmost importance to validate the functionality of CS deposits also under static and cyclic loading.

In this study, we have chosen Inconel 718, a Ni–Cr–Fe austenite super alloy, commonly used in aeronautics and energy applications, as a challenging material for cold spray deposition due to its high hardness. Inconel 718 is commonly used in various aerospace and energy applications because of its excellent creep properties and high corrosion resistance at elevated temperatures up to 700 °C. The exceptional properties of Inconel are mainly accredited to its intrinsic solid solution strengthening as well as precipitate strengthening [19,20]. Inconel as bulk material is rather expensive and difficult to machine caused by rapid work hardening; therefore, using AM technology can be helpful to reduce material waste and production cost of Inconel components. Several studies have been performed on the choice of process parameters (including laser power, laser scanning speed and direction, hatch distance, etc.) and microstructural and texture characterization of Inconel alloys fabricated by SLM in pure and composite formulations [21–26]. Zhang et al. [27] investigated the effect of various heat treatments on increasing the strength and hardness of SLM fabricated Inconel 718 samples, while significantly decreasing their ductility. Liu et al. [22], studied the effect of laser scanning path on mechanical and microstructural characteristics of Inconel 718 samples fabricated by laser solid form (LSF) technique. Amato et al. [28], investigated the effect of different post treatments including hot isostatic pressure (HIP) and annealing (1160 °C for 4 h) on the microstructure of SLM fabricated Inconel 718 samples. They reported comparable room temperature tensile characteristics of SLM samples with nominal properties of wrought and annealed alloy. Despite rather large number of studies performed on microstructure and static strength of SLM fabricated Inconel 718 samples, there is not so much data available in terms of fatigue strength of SLM fabricated Inconel alloys. The available fatigue studies are performed on stainless steel [29,30], aluminum alloys [31] and titanium alloys [32], and to the best knowledge of the authors no high cycle fatigue studies have been performed on AM fabricated Inconel 718 alloys. The only available data in the literature is the study performed by Kanagarajah et al. [33] who carried out low cycle fatigue tests on Inconel 939 at room temperature and 750 °C. The results

indicate that as built SLM samples had a better low cycle fatigue performance with respect to as cast material at room temperature, while the fatigue strength of as built SLM samples dropped dramatically at 750 °C presumably due to the fast formation of precipitates. Aging also was reported to reduce the low cycle fatigue strength of SLM Inconel 939 samples compared to cast samples at both room and high temperatures [33].

On the other hand, there are some studies on CS deposition of Inconel 718 in the form of coating. Marrocco et al. [34] were the first to report the possibility of obtaining quite dense Inconel 718 deposit by CS using different particle size; however, the deposited material was reported to display relatively low bonding strength of 13 MPa in the as sprayed condition. Wong et al. [35] studied the effect of particles velocity as well as successive heat treatment on the mechanical characteristics of Inconel 718 coatings. Higher spray velocity and high temperature heat treatments led to reduced porosity within the coating. Depending on the applied heat treatment and the selected CS parameters, tensile characteristics enhanced to varying levels displaying higher ductility with respect to the as sprayed material. Levasseur et al. [36] also reported limited strength and deformability of cold sprayed 718 deposits and adapted some pressureless sintering methods at varying temperatures and durations to enhance the mechanical characteristics of the deposited material. This post deposition sintering treatments gave rise to significant enhancement of the flexural strength and strain compared to the as sprayed material. More recently Singh et al. [37] investigated the effect of substrate roughness as well as spray condition on the deposition efficiency, microstructures, porosity and microhardness of Inconel 718 coating.

The functionality of freeform deposits of Inconel 718 obtained through CS deposition under cyclic loading is certainly a new topic that has not been investigated thus far. Even in case of SLM fabricated samples, most available studies are mainly focused on the static strength of the fabricated parts and there are actually very few studies on fatigue characteristics of AM samples prepared using SLM, with no studies focusing on fatigue strength of Inconel 718 alloys. The ever-growing demand for high quality AM parts for structural applications points toward the necessity of investigating their behavior under cyclic loading.

Herein, we evaluate the mechanical characteristics of freestanding Inconel alloy 718 samples fabricated by CS and SLM in as built and heat treated conditions. Our previous study validated the potential of CS to be used as an AM technique for fabrication of Inconel three dimensional objects [38]. In the present study, we focus on evaluating the static and high cycle fatigue characteristics of CS Inconel deposits as well as their fracture behavior and compare them with those of samples fabricated by an industrial SLM system. The obtained results have been also compared with the data available in the literature for bulk Inconel 718 fabricated by conventional manufacturing methods to better evaluate the efficiency of the exploited AM methods.

2. Experimental section

2.1. Material

Commercially available feedstock Inconel 718 powder used for fabrication of CS and SLM samples, supplied by Praxair Surface Technologies (USA) and H.C. Starck (USA) respectively had a particle size distribution of 10–32 μm and of 15–45 μm . Both powders displayed almost spherical shape whereas the one used for CS samples (Fig. 1(a)) represented a smoother surface morphology. The inserts in Fig. 1 exhibit the cross section of individual particles after chemical etching representing the typical dendritic microstructure of atomized powders.

2.2. Cold spray sample preparation

Inconel powder was sprayed on aluminum substrate using Impact

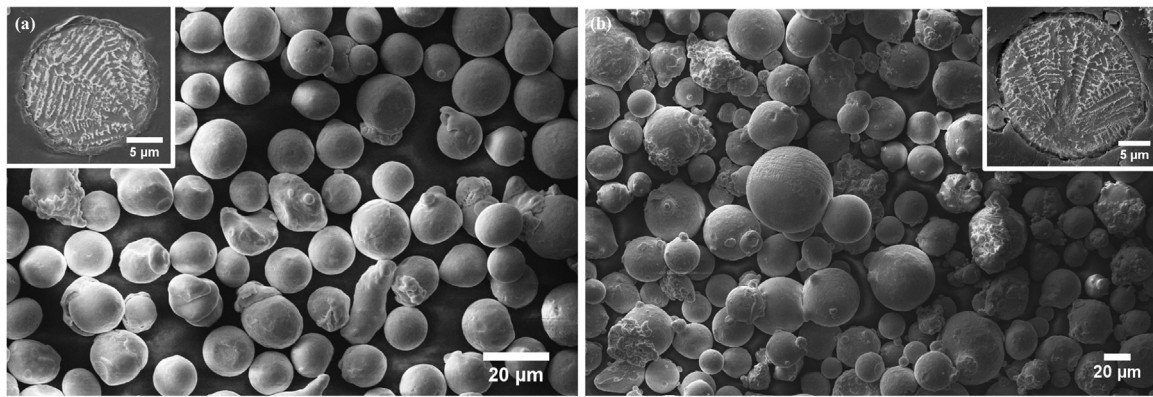


Fig. 1. SEM micrograph of Inconel 718 feedstock powders with the insert representing etched cross section of a single particle used for fabrication of (a) CS samples (b) SLM samples.

Innovation 5/11 (60 bar upgrade) spray system. Nitrogen, preheated to 1000 °C, was used as propellant gas at a pressure of 55 bar. The deposition was made at a traverse velocity of 500 mm/s and a track spacing of 1 mm with standoff distance of 25 mm. A coarse machining step was first performed on the depositions, followed by a finer finishing using Alzmetall milling machine and then the deposition was separated from the substrate in the final step. Tensile test samples were prepared following the geometry suggested by standard methods for tension testing of metallic materials (ASTM E8/E8M–15a) and samples for fatigue test were prepared following standard practice for conducting force controlled constant amplitude axial fatigue tests of metallic materials (ASTM E466 – 15). Our previous research confirmed that spray direction does not have any notable effect on the microstructure, porosity, microhardness and mechanical strength of CS depositions [38], thus in this study all samples have been prepared in the direction parallel to the spraying track.

2.3. Selective laser melting sample preparation

The samples were manufactured using a SLM® 280HL (SLM Solution Group AG) system equipped with 2 × 400 W Yttrium fiber lasers which work in parallel in a build chamber of 280 × 280 × 350 mm³. During the manufacturing process, the chamber was flooded with argon to reduce the oxygen content below 0.2%. Laser fluence defined based on the main process parameters including laser beam power (P), scan speed (v), hatch distance (h) and layer thickness (t), was defined as described in Eq. (1):

$$F = \frac{P}{v \cdot h \cdot t} \left[\frac{\text{J}}{\text{mm}^3} \right] \quad (1)$$

A layer thickness of 50 µm was used together with a fluence of 61.31 J/mm³ and a hatch distance of 0.17 mm. Rotation between subsequent layers is known to induce better overlapping and reduce anisotropic characteristics. Thus, a stripe scan strategy was adapted varying laser scan paths' orientation on each layer by 33°. Samples were manufactured heating the building platform up to 200 °C and in 90°, i.e. the sample's longitudinal axis (build direction) was parallel to the z-axis. Considering the anisotropy observed in previous tests, this direction was selected to consider worst case scenario in terms of mechanical strength for SLM samples. Samples were prepared with material allowance (0.5 mm) and subsequently machined according to ASTM E8.

2.4. Heat treatments

Different heat treatments were applied to the CS and SLM samples in order to homogenize the alloy elements and enhance their mechanical strength. For CS samples, the heat treatments were chosen to promote interparticle metallurgical bonding through sintering effect. Sintering has been practiced to enhance the mechanical strength of CS depositions

due to limited deformation of hard Inconel particles upon deposition [36]. Conventional sintering is normally performed at temperatures around 2/3 of material's absolute melting temperature, that is around 1260–1335 °C for Inconel 718 [35]. Accordingly, 1050 °C and 1200 °C were chosen as the peak temperatures of the two heat treatments HTA and HTB performed on both CS and SLM samples, as described in Table 1. For SLM samples, the two aforementioned treatments lead to very similar tensile strength data; thus, just HTB series was considered for further analysis. Then again, two other precipitation hardening treatments (HTC and HTD) were applied to SLM samples. HTC was applied following instructions of AMS5662 (aerospace material specification Nickel alloys) [39] for cast and forged Inconel 718. HTD samples, on the other hand, was considered as a stress releasing treatment for SLM samples subjecting them to just solution treatment (the first phase of HTC cycle) for a duration of 5 h.

2.5. Microstructural and mechanical characterization

Microstructural analysis was performed on cross section of samples, impregnated in hot mounting resin and ground with SiC papers up to P2500, followed by a micro-polishing step using diamond suspensions of up to 1 µm scratch size. After chemical etching, using 10 parts of HCl (37%) and 3 parts of H₂O₂ as etchant, the samples were observed by optical microscope at bright field mode and Zeiss-Evo 50 SEM microscope. X-ray diffractometer (XRD) phase analysis was performed on all samples, using Bragg-Brentano Philips PW1830/PW3020 XRD emitting CuKα radiation scanning (2θ) between 30° and 100° with an angular step and time per acquisition of 0.02° and 1 s/step respectively. The results were analyzed using X'Pert 1.3 and Match of Crystal Impact.

Porosity measurements were performed by analyzing SEM micrographs taken at backscattered electron imaging (BSI) mode on three random areas for each sample using ImageJ software [40]. A density determination kit (DDK) was also used to measure the density of the samples using the Archimedeian buoyancy principle (Precisa 100A-300M, Turin, IT). Briefly, samples were weighed in air and water; knowing the density of the water at controlled temperature, the density of the samples were obtained and porosity was calculated comparing the obtained data with the density of bulk material.

Microhardness was measured using microhardness tester FM-700 (Future-Tech, JP) with a diamond Vickers indenter applying a force of

Table 1
Description of applied heat treatments.

HTA	1050 °C for 3 h under argon atmosphere
HTB	1200 °C for 1 h under argon atmosphere
HTC	Max temperature of 980 °C following the heat/hold/cool cycle suggested in [39] for 24 h
HTD	980 °C for 1.5 h

300 gf and dwell time of 15 s. Residual stress field was characterized by AST X-Stress 3000 portable X-ray diffractometer (XRD) emitting $\text{CrK}\alpha$ radiation ($\lambda_{\text{Cr}\alpha} = 2.2898 \text{ \AA}$). $\text{Sin}^2(\psi)$ method was employed at diffraction angle of 128° for Inconel 718 (calibrated using microstrain free standard Ni sample at 133.5°), scanned with a total of 11 Chi tilts in the range of -45° to 45° along three rotations of 0° , 45° and 90° . Residual stress as well as full width of the diffraction peak at half of its maximum intensity (FWHM) profiles were obtained in depth through sequential material removal using electro-polishing with a solution of acetic acid (94%) and perchloric acid (6%). Tensile strength tests were performed following ASTM E8 specifications using a Universal MTS test system at a displacement rate of 2 mm/min. Force controlled constant amplitude axial fatigue tests with stress ratio $R = 0.1$ have been carried out at room temperature using Universal MTS test system at a frequency of 15 Hz on CS-HTA, CS-HTB, SLM-HTB and SLM-HTC series following the procedure described in ASTM E466-15. The up and down staircase method presented by Dixon and Massey [41] was followed to perform the tests with a stress step of 30 MPa. Both ISO 12107 (Metallic materials- Fatigue testing- Statistical planning and analysis of data) approach and Hodge–Rosenblatt [42] method were used for analysis of fatigue test data and assessing fatigue strength corresponding to a fatigue life of 2 million cycles. Each fatigue test series included 11 samples. Fractography analysis on fracture surface of failed fatigue samples were performed using a Zeiss-Evo 50 SEM microscope.

3. Results

3.1. Microstructural characterization

The optical micrograph of CS samples' cross section (Fig. 2 (a)–(c)) present highly deformed splats as the characteristic features of cold spray process. Fig. 2(a) shows a dendritic structure inside the splats, similar to the original tree-like microdendritic structure of the rapidly solidified powder crystals shown in the insert of Fig. 1(a). This dendritic structure tends to fade after heat treatments (Fig. 2(b) and (c)) developing a more uniform and homogeneous microstructure.

Fig. 2(d) and (e) represent the microstructure of the As-built SLM sample on cross sections parallel and perpendicular to the build direction respectively. Fig. 2(d) illustrates the development of layers comprised of arc-shaped molten pool boundaries with an average max height of $115 \pm 22 \mu\text{m}$. Columnar dendrites are observed generally growing along the build direction, mostly traversing through few melt layers. The general appearance of the section parallel to the scanning plane, Fig. 2(e), shows a cellular and dendritic structure organized in a way that highlight the direction of multiple laser tracks with 33° rotation between the adjacent layers. Fig. 2(f)–(h) show the perpendicular to the build direction cross section of SLM samples after different heat treatments. In all three cases, the laser scan traces almost disappeared after heat treatment; however, each heat treatment has resulted in a different but unevenly distributed grain structure. An apparent recrystallization can be observed through the cross section of HTB sample, exhibiting much coarser grains (note the scale bar in Fig. 2(f)). After HTB, the dendritic structure is completely dissolved and fully substituted by uneven mixture of fine and coarse equiaxed grains. SLM-HTC, on the other hand, represents a more uniform distribution of grain size with visible traces of dendritic structure; The grain size distribution in SLM-HTD samples is more similar to that of SLM-HTB, but with apparently less defined grain boundaries.

SEM observation and XRD profiles of cold spray samples are represented in (Fig. 3). The XRD patterns of as sprayed CS samples indicate the presence of γ phase. Comparing the interplanar spacing and reticular parameters of the CS-as sprayed, CS-HTA and CS-HTB (provided in Supplementary material), an average reduction is observed for the heat treated series compared to the as sprayed one. This reduction could be attributed to phase precipitation that tends to deplete the solid solution γ phase from the alloying elements after heat treatments [43].

The difference between the XRD pattern of CS-HTA sample and that of CS-as sprayed one, is an alteration in the intensity of the phase γ (Ni), in particular in correspondence with the peak at 2θ of 50.6° (200) planes that could be due to a preferential orientation and a displacement of the peaks, which is in line with the variation of the lattice parameters. There are also four quite low intensity peaks that could correspond to the (Nb, Ti) carbides. This hypothesis is in agreement with the SEM observation (Fig. 3(a)–(c)) and the EDS analysis performed on the precipitates. These precipitates represent a morphology compatible with that of (Nb, Ti)C phase [44]. No notable difference was detected between the XRD patterns of CS-HTA and CS-HTB samples.

In case of SLM samples, the dominant identified phase is again the γ phase. No significant difference was observed between the reticular parameter of the γ phase between differently treated SLM samples; i.e. average a_0 of 3.605 \AA for as built and HTD series and 3.601 \AA for HTB and HTC (provided in Supplementary material). SLM-HTB sample shows quite clear sideband on the lower angle side of γ phase peaks particularly at 2θ of 74° , 90° e 95° . Comparing these sidebands with what is reported in the literature [45], they could be attributed to segregation of Nb leading to formation of micro regions of Nb rich austenite. There is also one peak at 2θ of 35° that can be attributed to (Nb,Ti) carbides. SLM-HTC sample, on the other hand, exhibits additional phases with peak positions and corresponding interplanar spacing reported in Table 2. For comparison, the interplanar spacing of principal reflections reported in the literature for Inconel 718 are also included [44,45]. Sample SLM-HTD shows a XRD pattern very similar to that of the as built SLM sample. The three peaks detected at 2θ of 35° , 23° ($d = 2,5475 \text{ \AA}$), 40.8° ($d = 2,2117 \text{ \AA}$) and 45.35° ($d = 1,9998 \text{ \AA}$) could be caused by the formation of carbides.

3.2. Porosity measurements

BSI-SEM micrographs of the polished cross sections, shown in Fig. 4, were used for porosity evaluations. CS samples were found to generally have higher porosity with respect to the SLM series, although porosity of CS series tend to decrease after heat treatments. This observation is confirmed also by volumetric porosity measurements performed by DDK. Fig. 4(d)–(g) represent the polished lateral cross sections of SLM samples before and after heat treatments. As built SLM sample represented few pores or cracks that were more visible in the lateral cross section (perpendicular to the build direction) compared to the one parallel to the build direction (not presented for the sake of brevity). Overall, high density and few sparse individual pores were observed in cross sections of SLM samples.

Average data obtained from image analysis on three different areas per sample series as well as the DDK measurements for three samples per series are presented in Fig. 4(h). Image analysis and DDK data show similar trends confirming the positive effect of heat treatments in reducing porosity of CS samples; whereas the effect of heat treatment on porosity of as-built SLM series was trivial. It is to be noted that no porosity was observed at BSI-SEM images of feedstock powders (inserts in Fig. 1).

3.3. Microhardness measurements

Microhardness was measured across lateral cross sections of CS and SLM samples perpendicular to the spray and the build direction before and after different heat treatments. The results showed uniform hardness distribution throughout the cross section of all samples, thus average data for three measurements on each cross section are reported in Fig. 4(i). The CS sample showed the highest microhardness due to the extreme work hardening effect of the impact to the substrate/successive splat layers; however, the hardness value was markedly reduced after both heat treatments, without notable difference between the resultant microhardness from HTA and HTB. SLM samples, on the other hand, exhibited a remarkable increase of over 40% in the microhardness after

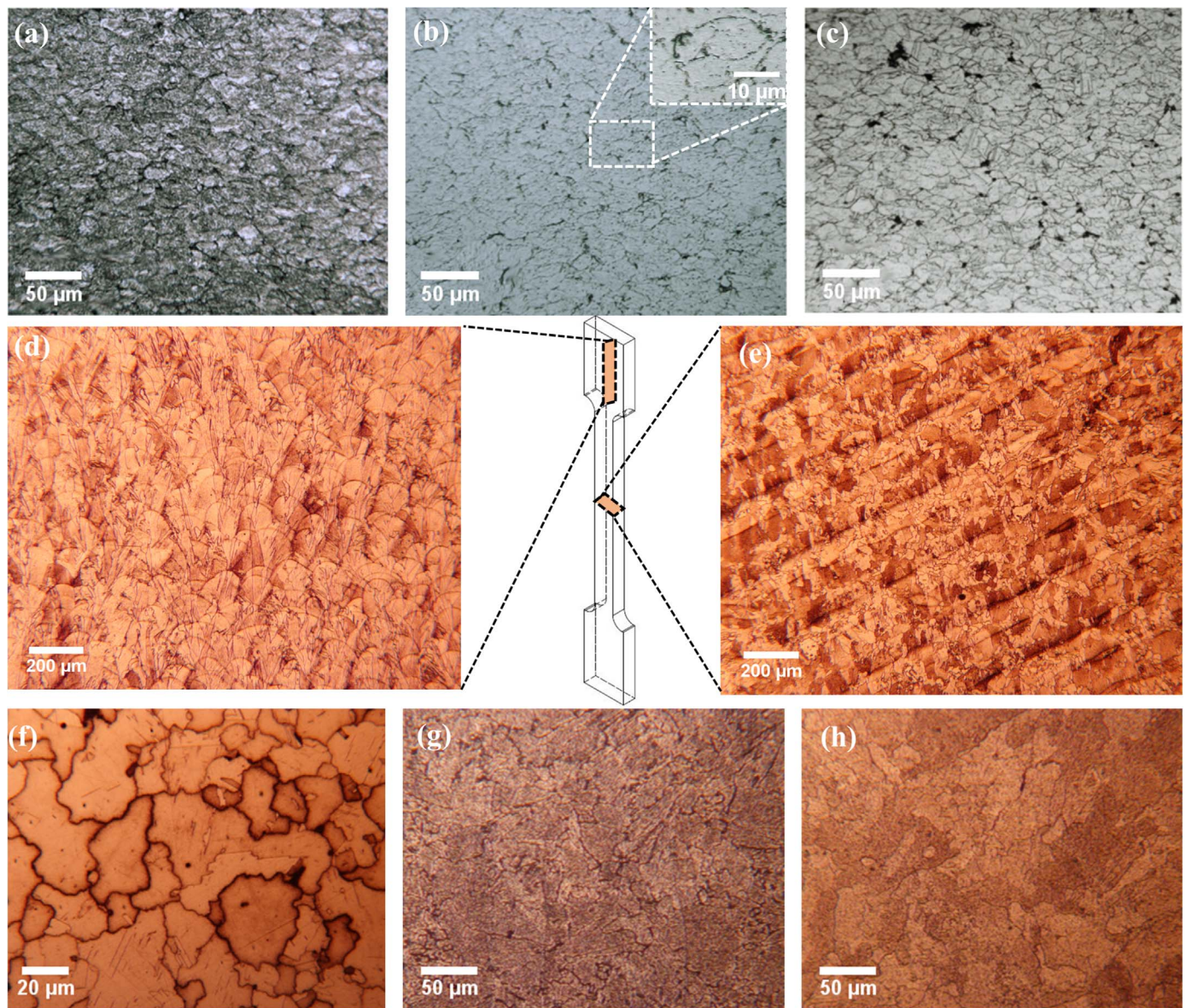


Fig. 2. Optical micrograph of samples cross sections after chemical etching (a) CS (b) CS-HTA (c) CS-HTB (d) SLM-As built parallel to the build direction (e) SLM-As built perpendicular to the build direction (f) SLM-HTB (g) SLM-HTC (h) SLM-HTD.

heat treatments HTB and HTC; while HTD represents a lower microhardness increment. It is to be noted that microhardness reported in the literature for bulk material (cast or wrought Inconel) ranges between 230 and 380 HV [39,46].

3.4. Residual stress distribution

Surface and in depth XRD measurements provided the distribution of residual stresses as well as FWHM trend in CS and SLM series' lateral cross section, as presented in Fig. 5. The measurements exhibited almost no residual stresses in CS sample in the as sprayed format; however, compressive residual stresses were measured on CS samples after machining, before and after heat treatments. In case of SLM series, as built sample showed considerable tensile residual stresses that can have an adverse effect on the fatigue strength of these series. SLM-HTC and SLM-HTD samples display negligible compressive residual stresses and highest compressive residual stresses are obtained after HTB treatment, which also in this case can be considered quite local and affecting just the surface layer (to a depth of 0.08 mm).

The trends of FWHM parameter, which can be regarded as a

cumulative index of hardness, grain size as well as microstrain are separately presented for CS and SLM series in Fig. 5(c) and (d) respectively. In case of CS samples, the FWHM exhibits similar values for as sprayed and machined series and clearly depicts the softening effect of the applied heat treatments on CS samples. The quite similar FWHM values measured on CS-HTA and CS-HTB samples are in agreement with the comparable microhardness data for these two series (Fig. 4(i)). SLM samples present lower FWHM parameter in general compared to the CS series, and these values tend to decrease after heat treatments, with SLM-HTB showing the lowest trend for FWHM parameter.

3.5. Static tensile strength

Engineering stress strain graphs, displayed in Fig. 6(a), point out that CS samples have quite low tensile strength and ductility before heat treatment; the applied heat treatments induce a transition from entirely brittle characteristics of CS sample to a quite ductile behavior in CS-HTA and CS-HTB series. The ultimate tensile strength (UTS) and the ductility of the CS samples were significantly enhanced after heat treatments; Table 3, which summarizes the tensile test data, shows a

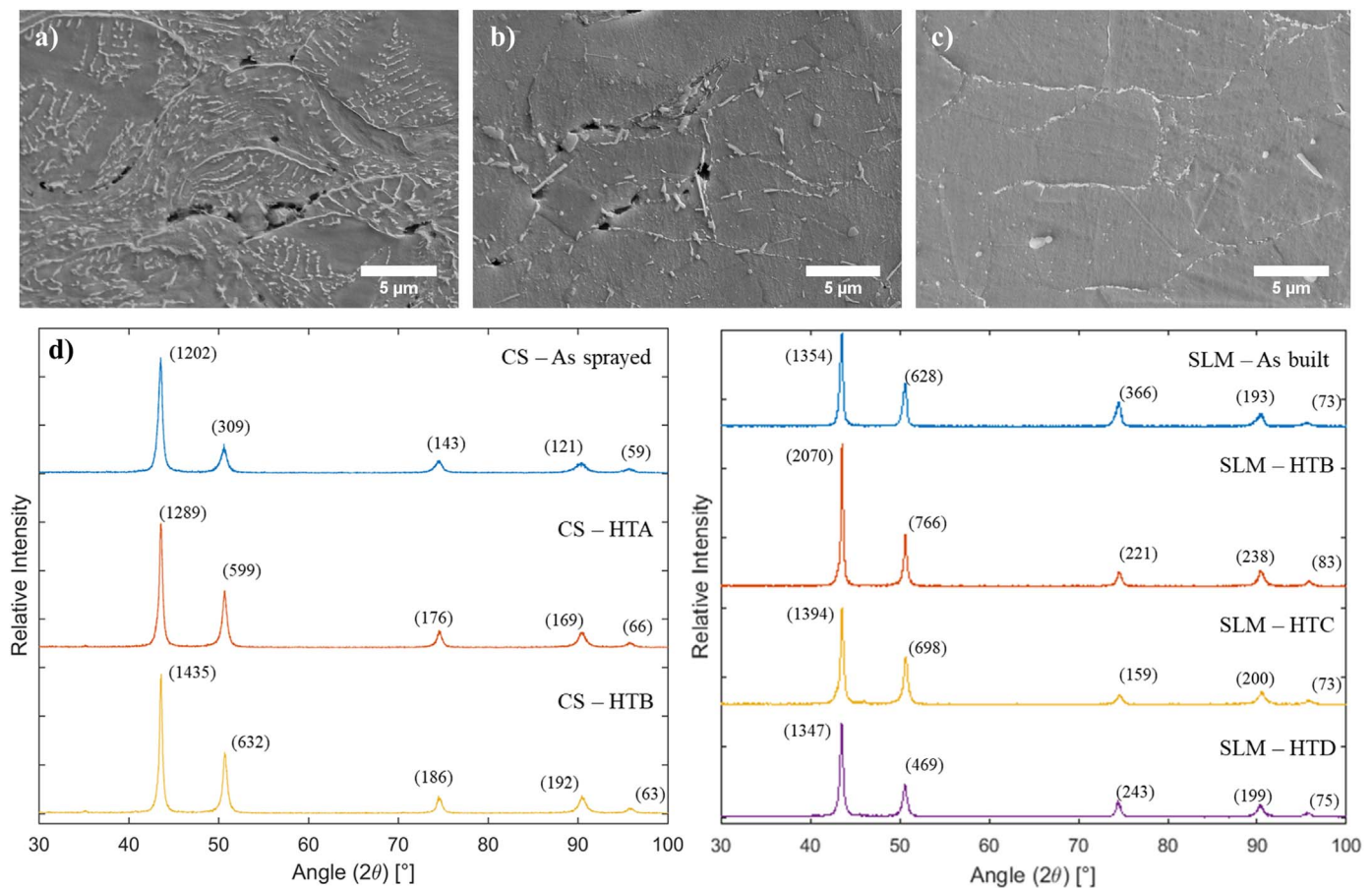


Fig. 3. SEM cross sectional observation (a) CS (b) CS-HTA (c) CS-HTB and (d) XRD profiles of CS and SLM samples.

Table 2

Interplanar spacing calculated from the peaks other than γ phase peaks for SLM-HTB sample.

Detected phases			(Nb, Ti)C		δ		γ''	
2θ	d	Possible phase	d [44]	d [44]	d [43]	d [44]		
35.15	2.5532	(Nb, Ti)C	2.549	2.103	2.107	2.098		
40.6	2.2221	(Nb, Ti)C	2.212	1.989	1.852	1.843		
43.07	2.1002	δ	1.566	1.965	1.812	1.807		
45.44	1.9961	δ	1.336	1.291	1.294	1.294		
46.09	1.9694	δ	1.28	1.271	–	–		
58.83	1.5697	(Nb, Ti)C	–	1.193 (VFW)	–	–		
80.55	1.1926	δ (VFW)	–	–	–	–		

notable elongation of 15% obtained for CS-HTB series. SLM samples with no heat treatment show a rather high ductility, while the latter together with SLM-HTD series exhibit the lowest strength among all series. The UTS and yield strength of SLM samples considerably enhanced after HTA, HTB and HTC but at the expense of losing ductility. Amid the tested series, SLM-HTA and SLM-HTB represent the best combination of mechanical strength and ductility, exhibiting very similar tensile characteristics. Hereinafter, SLM-HTB series was considered as the representative treatment of the two, showing slightly higher strength and comparable ductility with respect to SLM-HTA. According to the data presented in Table 3, the ductility obtained for SLM, SLM-HTA, SLM-HTB and CS-HTB series are comparable with the data available for bulk material in a wide array of heat treatments and aging conditions [21,47–50].

3.6. Axial fatigue strength

To the best of our knowledge, there is no data available in the literature for bulk Inconel 718 axial fatigue test at room temperature and the few available room temperature fatigue data are for rotating bending fatigue tests with stress ratio of $R = -1$ performed on materials that vary widely in terms of the applied heat treatment. For examples the data presented in [51] corresponds to solid-solution treated rolled round bar (13 mm in diameter) 718 alloy, heated at 982 °C for 1 h and water quenched, aged at 720 °C for 8 h, furnace cooled to 621 °C, aged at 621 °C for another 8 h, and lastly exposed to air cooling; the other set of data used for comparison is obtained for cantilever-type rotary bending fatigue tests carried out at room temperature on Inconel samples with a similar heat treatment described above [52]. The data reported in [53] is for Inconel 718 plate, with comparable thickness to our samples, hot rolled at 1000 °C/1 h and aged at 700 °C/8 h. In order to be able to compare these room temperature rotating bending data with our tests condition (axial fatigue tests with $R = 0.1$), Goodman diagram [54] was constructed using the mechanical properties and fatigue limits reported in the literature for the aforementioned studies. The literature data decoded by High diagram are presented in Fig. 6(b) and Table 4 using both calculation methods (ISO 12107:2012(E) and Hodge–Rosenblatt). The stress values refer to the stress amplitude at the reduced area of the samples.

3.7. Fractography analysis

Fractography of tensile test samples previously confirmed entirely brittle features comprised of inter-splat and intra-splat rupture modes on fracture surface of CS samples, versus clearly visible ductile features on as built SLM ones [38]. Here we have compared the fracture surface

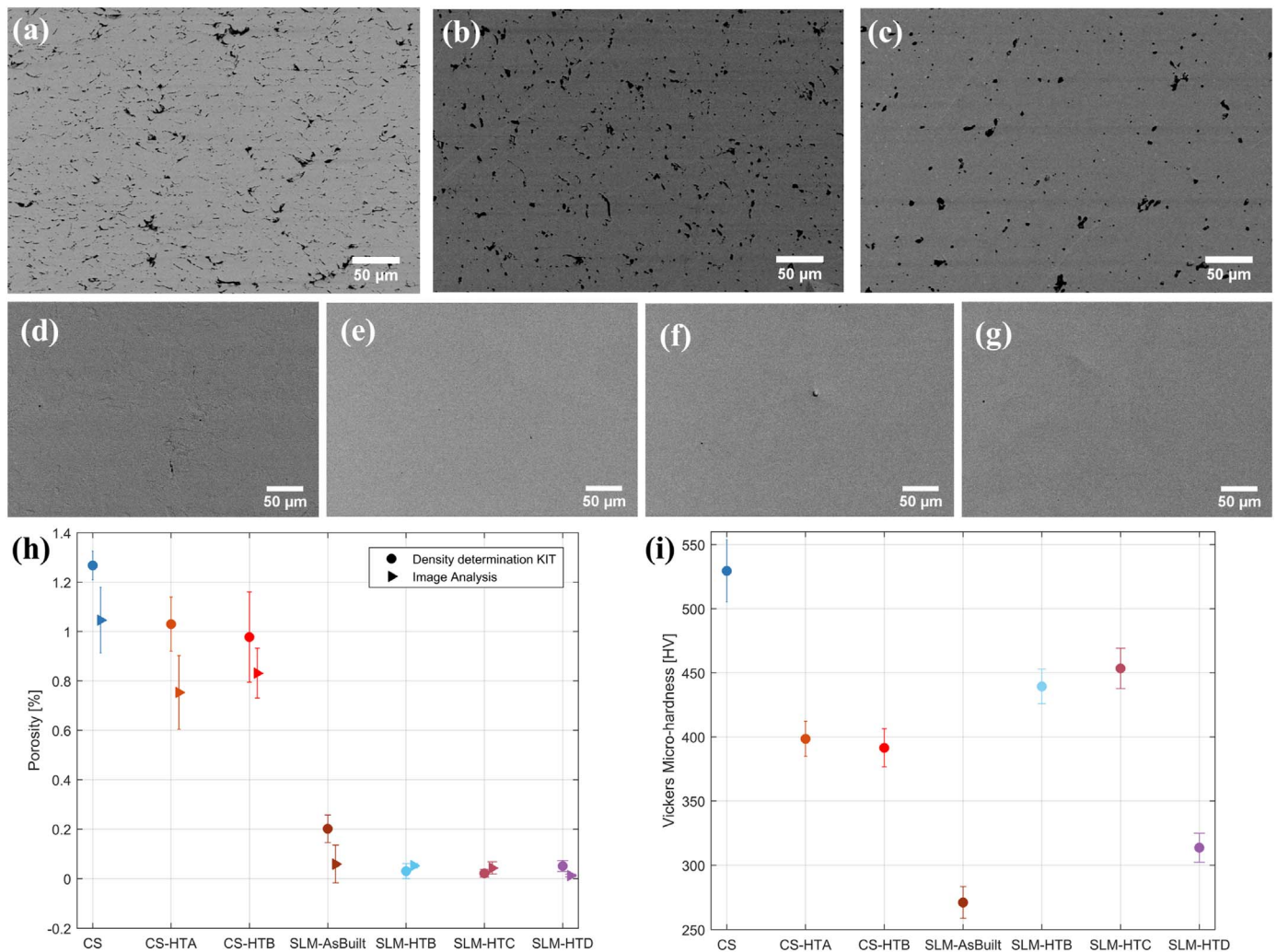


Fig. 4. BSI-SEM micrographs of samples cross section for porosity measurement (a) CS (b) CS-HTA (c) CS-HTB (d) SLM-as built (e) SLM-HTB (f) SLM-HTC (g) SLM-HTD (h) porosity data in CS and SLM samples performed by image analysis and density determination kit (i) microhardness data obtained on the cross section of CS and SLM samples.

of heat treated fatigue tested samples. Fracture surfaces of CS samples after heat treatments represent combined brittle and ductile fracture mechanism, exhibiting both areas with whole split detachment (Fig. 7(a)) and areas covered with micro-dimples (Fig. 7(b)), that are characteristics of ductile fracture. The fraction of the total fracture area covered by dimples and tear ridges seem to increase after HTB treatment compared to HTA.

Fracture surface of SLM-HTB samples, alternatively, represent uniformly dispersed ductile features highlighting a dominant ductile mechanism of failure. Fatigue crack initiation sites were generally identified close to the samples' surface (Fig. 7(c)). Closer look to the surface features confirm the presence of tiny dimples pointing out transgranular ductile failure mode. SLM-HTC samples, on the other hand indicate the presence of various pores, cracks or un-melted powders on the fracture surface, despite the global transgranular ductile failure mode characterizing the fracture surface.

4. Discussion

Limited machinability of nickel super alloys imposes several technical obstacles for conventional, subtractive fabrication methods. Precipitation strengthening and solid solution strengthening of molybdenum and niobium elements in the nickel-chromium matrix are known to be responsible for significant hardness, low thermal conductivity and notable work hardening rates which make it challenging

to use subtractive fabrication methods for Inconel [26,55]. Thus AM can be considered as an apt solution for fabrication of complex shaped Inconel structural components, for the prospect of reducing production costs and to reduce the scrap material resulting from machining. The application of CS as an AM method in this case has the particular advantage of being an extremely material effective solution.

Herein, we used two powder based AM methods of CS disposition and SLM to fabricate standard Inconel test samples and evaluate the potential of CS to be used as an AM technique rather than just an efficient spray coating method.

CS and SLM samples were fabricated using commercially available Inconel 718 powders and different heat treatments, based on sintering indications or the standard recommendations for wrought material, were applied with the aim to homogenize the microstructure, enhance mechanical properties and/or release the undesired residual stresses. The microstructure of the feedstock powders in both cases exhibited a dendrite structure typical of atomized powders with presence of no pores or microdefects across the cross section (Fig. 1). CS samples' microstructure, which was previously assessed to be independent from spray direction [38], exhibited uniform presence of dendritic structure throughout its cross section (Fig. 2(a)), confirming that initial microstructure of the powders was preserved through CS process. After heat treatments, the dendritic structure inside the highly deformed splats almost vanished and the inter-splat boundaries tended to fade (Fig. 2(b) and (c)). The latter observation was promoted by some partial sintering

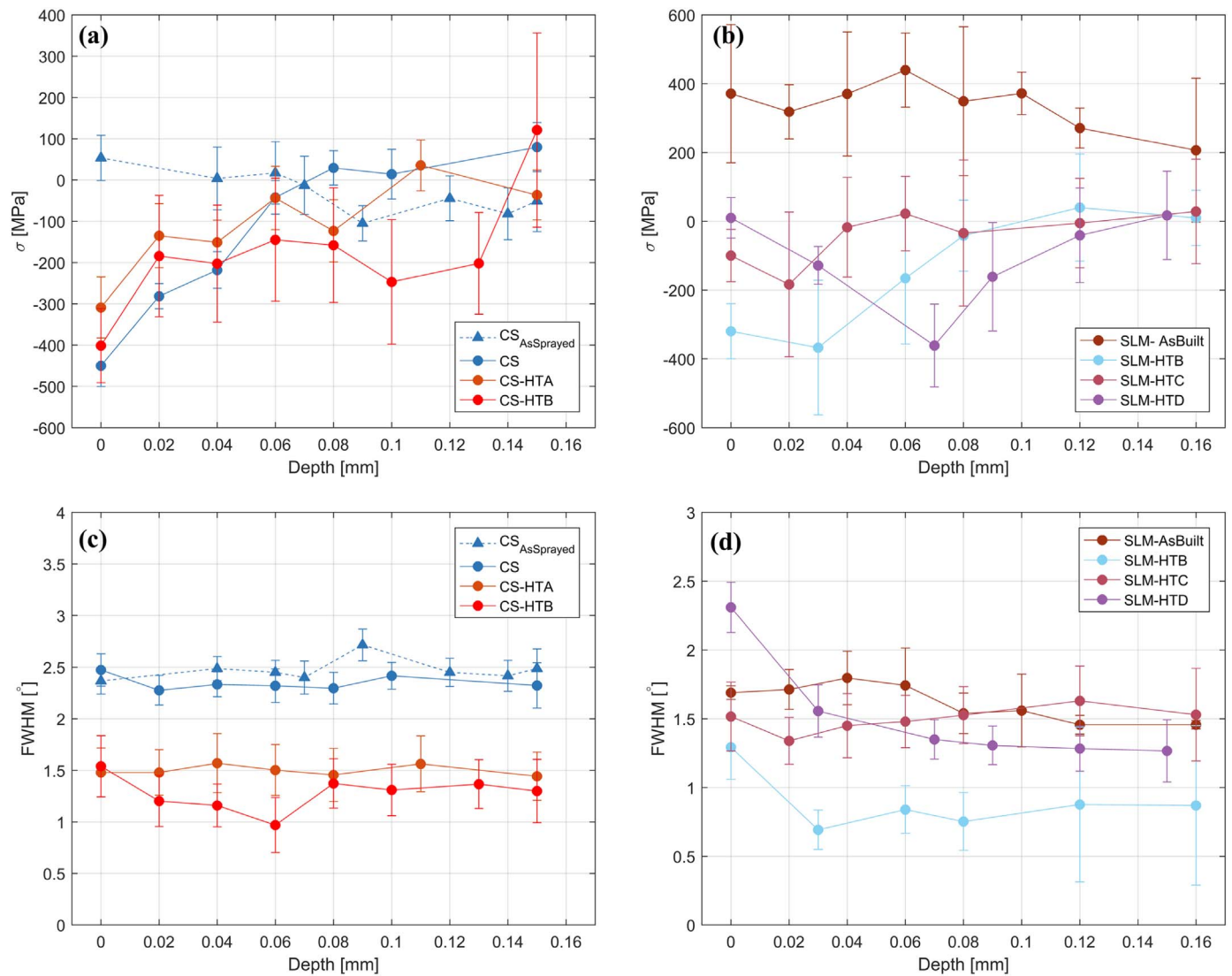


Fig. 5. Distribution of residual stresses and FWHM in depth respectively for (a) and (c) CS samples (b) and (d) SLM samples.

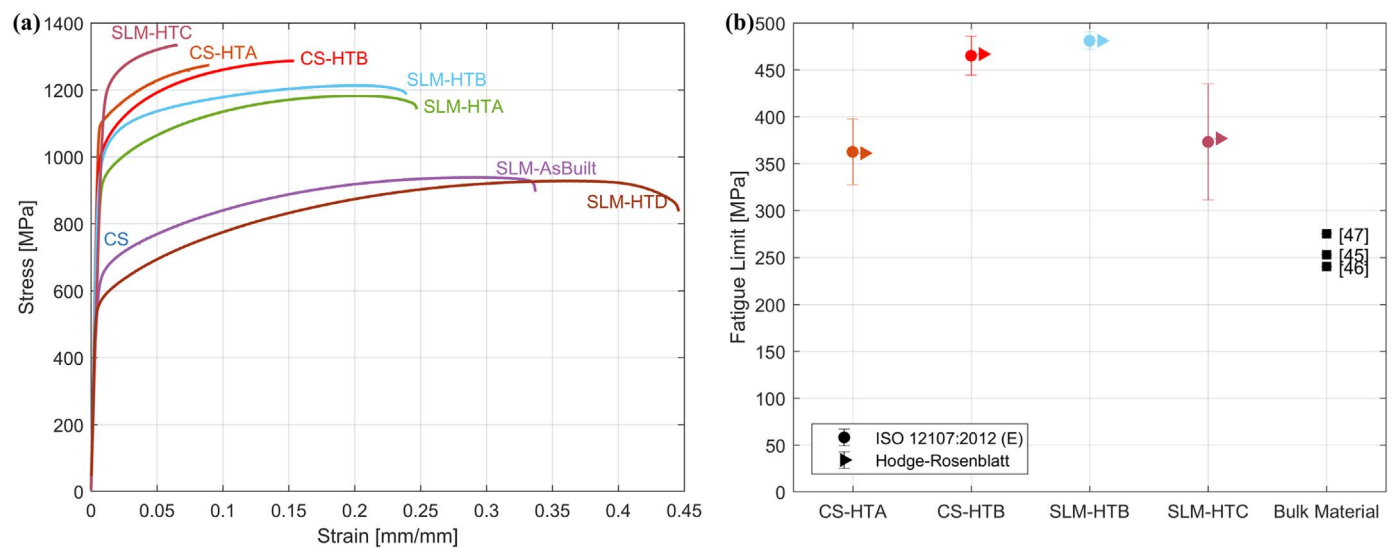


Fig. 6. (a) Representative engineering stress strain graphs of CS and SLM samples before and after various heat treatments (b) fatigue strength corresponding to 2 million cycles for CS and SLM samples compared to the bulk material fatigue test data available in the literature decoded for stress ratio of $R=0.1$ using Haigh diagram.

Table 3
Tensile test data for SLM and CS samples.

	CS	CS HTA	CS HTB	SLM	SLM HTA	SLM HTB	SLM HTC	SLM HTD	Bulk Material [21,47–50]	Cast AMS5383 [27]	Wrought AMS5662 [27]
Ultimate tensile strength (MPa)	713 ± 11	1260 ± 26	1289 ± 2	943 ± 8	1186 ± 2	1210 ± 23	1339 ± 30	933 ± 3	≥ 1000	862	1276
Yield strength (MPa)	–	1087 ± 24	1004 ± 7	596 ± 30	924 ± 11	951 ± 3	1158 ± 14	558 ± 7	≥ 800	758	1034
Young's modulus (GPa)	167 ± 7	191 ± 9	202 ± 2	170 ± 9	158 ± 17	195 ± 2	138 ± 6	170 ± 7	200	–	–
Strain at break (%)	0.45 ± 0.1	8.85 ± 0.3	15 ± 1	35 ± 1	25 ± 5	23 ± 1	7 ± 1	43 ± 1	≥ 18	5	12

Table 4
Fatigue test data.

Fatigue strength corresponding to 2 million cycles [MPa]	CS-HTA	CS-HTB	SLM-HTB	SLM-HTC	Bulk material data
Hodge – Rosenblatt	361	467	481	377	253 [51]
ISO 12107:2012(E)	363 ± 35	435 ± 26	481 ± 9	373 ± 62	275 [52] 184 [53]

effect after heat treatments. Two different types of boundaries were identified between the splats of heat treated samples, as shown in the higher magnification insert in Fig. 2(b): continuous interparticle boundaries observed between individual splats and the sporadic boundaries that were observed throughout single particles. The presence of primary and secondary splat boundaries were reported also on cold sprayed Inconel 625 alloy [56]. The well-defined primary

boundaries at the particles interface are known to be caused upon high kinetic energy impact between individual particles during deposition process, whereas the incomplete secondary boundaries are formed due to the severe plastic deformation and the consequent increase in defect density and dislocations within individual particles. Several deformation twin boundaries can be observed in CS-HTB sample, which can be attributed to the partial recrystallization after heat treatment.

SLM as built samples represent essentially different microstructural features in the observations parallel and perpendicular to the build direction, respectively highlighting the features created by the adjacent solidified molten pools formed during layer development and the laser tracks following the stripe scan strategy (Fig. 2(d) and (e)). Both parallel and perpendicular sections exhibit regular columnar dendrites; In Fig. 2(d), the dendritic structures show a preferential direction elongated along the build direction, some traversing through several layers following the heat dissipation direction during the molten pool solidification. The columnar dendrites are not found to be perfectly parallel

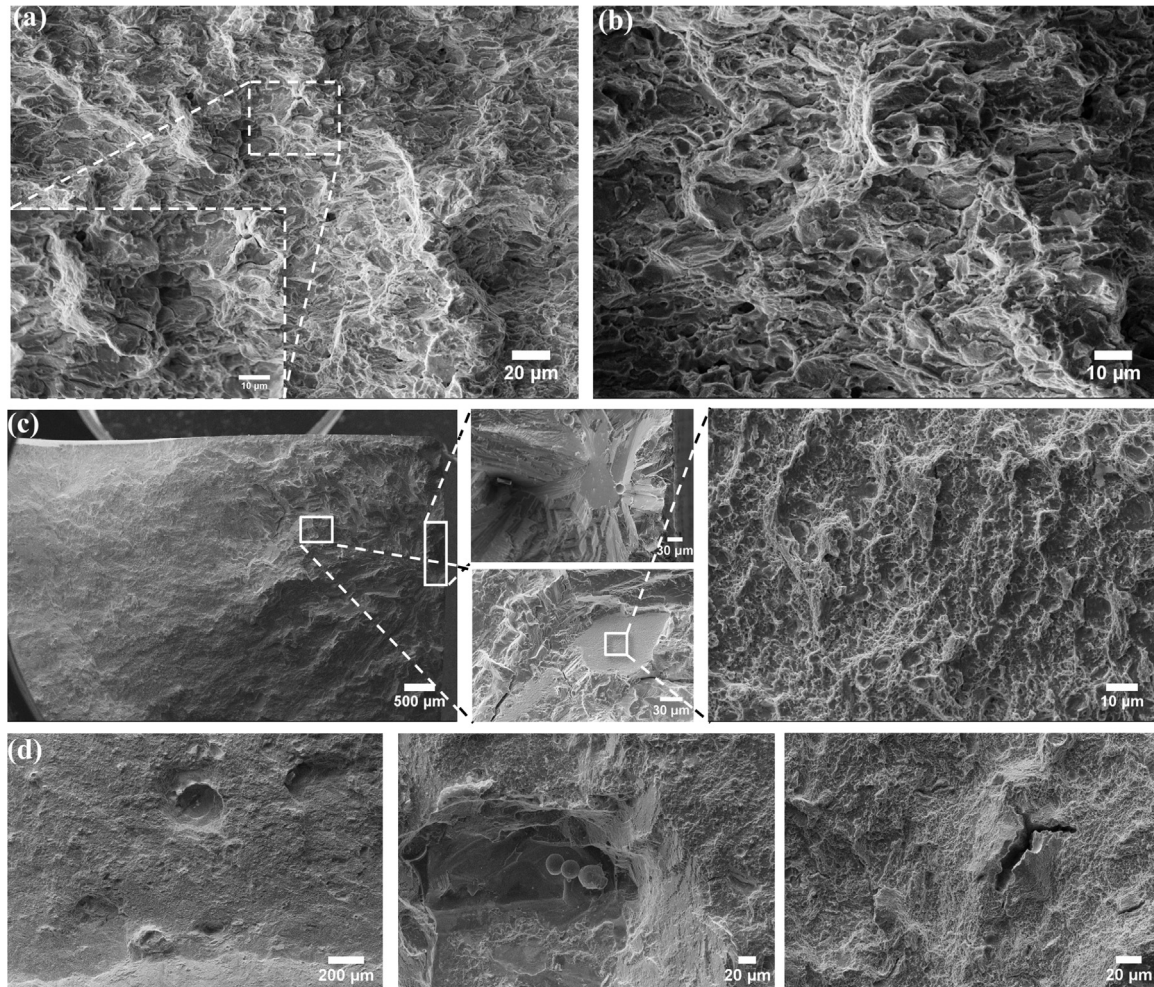


Fig. 7. Fractographic observation of fatigue tested samples (a) CS-HTA, (b) CS-HTB, (c) SLM-HTB (d) SLM-HTC.

probably caused by the intricate heat flow history during the SLM route. Heat treatments result in evident recrystallization in all SLM series; however, SLM-HTB sample represents total disappearance of the dendritic structure through uneven distribution of grain size, while SLM-HTC partially preserves the original dendritic structure and maintains a rather uniform grain size distribution. SLM-HTD, on the other hand, shows a grain size distribution more similar to that of SLM-HTB series with traces of the dendrites still present throughout the matrix. The uneven grain size distribution was observed also by Zhang et al. [27] during solution annealing of Inconel samples. They attributed this irregularity to uneven distribution of residual stresses in micro areas between the overlapping of neighboring laser tracks, where higher residual stresses provide higher driving force for recrystallization compared to the areas with lower residual stresses. Similar results were reported also in [57].

XRD phase analysis of CS samples showed the effect of heat treatments in promoting phase precipitation that leads to deplete the solid solution γ phase from the alloying elements, as also confirmed by SEM analysis. HTA and HTB led to quite similar results on CS samples. The γ phase was the dominant phase identified also for all SLM series. Formation of sidebands on the lower angle side of SLM-HTB peaks could indicate Nb segregation in the γ matrix, considering the lattice parameter of the Nb rich region. SLM-HTC samples showed a more notable phase transformation among all series, while the results of SLM-HTD series was quite similar to that of SLM as built series considering also the milder heat treatment they went through. Variation in tensile strength properties could be attributed to the possible phase transformation as well as carbide formation and segregations after the applied heat treatments.

Porosity measurements performed by image analysis of the BSI-SEM micrographs and the DDK, showed much higher porosity for CS samples compared to the SLM ones (Fig. 4(h)). The higher measured porosity of CS series, as illustrated in Fig. 4(a)–(c), is mainly caused by the limited deformability and compaction of the hard Inconel powders upon impact. Oxide layer on the powder's surface and imperfect surface morphology of powders can also contribute to form micro-porosities and inadequate interpenetration between neighboring splats [58]. Pore reduction in CS samples after heat treatments can be recognized as a direct effect of the high annealing temperature that enhanced inter-splat bonding due to the sintering effect introduced within the sample's matrix. Alternatively, all SLM series, show almost fully dense cross sections apart from few local pores and some microdefects in the SLM as built sample that seem to have been eliminated after heat treatments. The difference between the data obtained from cross sectional image analysis and the DDK can be principally attributed to the inherent differences between these two approaches; that is DDK provides information about the volumetric porosity, while image analysis is representative of the cross sectional porosity. Image analysis can also offer data about the distribution and morphology of the pores along the cross section. Overall, the porosity of the CS deposited samples, although higher than that of SLM series, was as low as 1%. This high density can be ascribed to the severe plastic deformation upon impact caused by the high kinetic energy of the powder particles at their critical velocity, backed up with the subsequent heat treatments that promoted metallurgical bonding.

Microhardness measurements confirmed a rather homogeneous distribution across the section of all samples, regardless distance from the boundaries. Significantly different hardness values of CS and SLM samples before heat treatments are mainly caused by the intrinsic differences of the processes that resulted in essentially different microstructures. Severe plastic deformation caused by the high energy impact of particles during CS process results in high density of dislocation and hence increases the microhardness, which tends to decrease after heat treatments; whereas, particle melting and subsequent solidification during SLM process can cause grain growth and material softening. The obtained data for heat treated CS samples, indicate that the reduced

porosity of the heat treated CS samples has not been enough to counteract the softening effect of the heat treatments and both applied heat treatments reduced the matrix hardness in CS samples almost 25%. For all heat treated SLM samples, the hardness, however, enhanced significantly due to the solution strengthening and formation of precipitations as reported also in [28] to different extents depending on the applied heating/cooling cycle. All the CS and SLM samples, nevertheless, showed comparable and in most cases higher microhardness compared to the conventionally fabricated bulk material.

The XRD measurements revealed negligible residual stresses in the CS-as sprayed samples, in spite of the high energy impacts of the powder particles which were expected to induce compressive residual stresses. Indeed, the absence of compressive residual stresses in as sprayed samples, points out to the machining process as the source of compressive residual stresses in the machined CS series, which turned out to have induced high stresses just close to the surface that fade out at a depth of 0.06–0.08 mm. Thus the obtained results here in case of CS-as sprayed samples indicate that the gas temperature has highly overshadowed the favorable effect of successive impacts with high kinetic energy for inducing compressive residual stresses [59,60]. For SLM samples, on the other hand, the irregular temperature field that the material experiences during repeated heating/cooling cycles through the fast and repetitive passage of laser tracks can lead to a sharp stress gradient. This is known to induce thermal residual stresses (Fig. 5(b)). After the heat treatments, notable relaxation of residual stresses is observed. In some cases, particularly SLM-HTB, even compressive residual stresses are measured close to the surface to a depth of 0.06 mm. We postulate that this observation could have been caused by formation of precipitates during the applied heat treatments.

Differences in the mechanisms of CS and SLM can be considered the reason behind higher FWHM values in as sprayed and as machined CS samples with respect to the SLM ones before heat treatment.

In fact, FWHM can be correlated with three factors: the instrumental broadening, the grain size and the microstrains. Since the same instrument was used for all the measurements and the broadening effect was subtracted through calibration with a microstrain free standard powder, the alterations in FWHM can be attributed to the grain size and the microstrain. The dynamics of CS affirms that grain refinement and microstrains are both strictly related to the process itself while as regards SLM, since thermal instead than kinetic energy is used, larger grain size as well as smaller microstrains are expected. That is to say that when kinetic energy is used as the source for deposition, smaller grain size and surface work hardening with an associated higher hardness is expected, whereas if thermal energy is used, a more ductile and less resistant material is achieved.

After heat treatments, however, the exposure to high temperature recovers ductility and results in lower hardness and lower FWHM values in CS samples.

Tensile test data represented substantial increase in elongation of CS samples after heat treatments. The enhanced cohesive strength and the transition from a rather brittle behavior to a mixed brittle-ductile failure mode, as also confirmed by the fractography observations (Fig. 7(a) and (b)), is attributed to the enhanced inter-splat metallurgical bonding that was promoted by the choice of heat treatments. Notable increase in mechanical strength of CS samples after heat treatments, indicate the major role of microstructure, interparticle bonding as well as improved structural homogeneity and pore reduction.

The SLM samples exhibited increased strength and decreased ductility after HTA, HTB heat treatments. The enhanced strength can be attributed to the precipitation strengthening mechanisms at high temperatures. Whereas, the precipitation hardening activated at high temperatures reduced ductility and thus elongation. Similar observations were reported in [27], where different phases of precipitates in Inconel 718 were accounted responsible for reduction in ductility. SLM-HTC samples represent the highest strength among all series, most

probably caused by the solid–solution and precipitation strengthening, the considerably lower ductility of this series can also be attributed to the precipitates formed during the cycle of this heat treatment, which induced some brittleness in the material matrix. Similar trend was reported for different solution aged and homogenized + solution aged SLM Inconel 718 samples, where the combination of enhanced strength and reduced ductility was attributed to the strengthening precipitated of γ' (Ni₃(Al,Ti)) and γ'' (Ni₃Nb) and needle-like δ phases. The latter is reported to prevent dislocation motion and consequently result in lowered ductility [26,27]. HTD that was applied with the intention to release stresses, did not significantly change the mechanical properties apart from marginally increasing elongation with respect to the SLM as built material.

While the CS and SLM as built samples had lower UTS compared to bulk material, all the heat treated series, except SLM-HTD, exhibited comparable UTS with wrought and cast Inconel. In terms of elongation, CS-HTB, and all SLM series except SLM-HTC, showed comparable or exceeding ductility compared with nominal data available for the bulk material. Overall, the heat treated CS and SLM series meet the requirements for Aerospace Material Specification for cast and wrought Inconel 718 alloy [27].

Investigating fatigue strength of CS fabricated samples is of utmost importance to verify their potential for application as structural components rather than deposited coatings, or being used for repair purposes or geometrical restoration of unloaded mechanical components, as CS has been basically used thus far. Constant amplitude axial fatigue tests with stress ratio of 0.1 carried out on different heat treated series of samples, confirmed that with proper heat treatment, CS samples can exhibit a notable fatigue strength that is not only comparable with the SLM samples but also with that of conventionally fabricated bulk material. According to the fractographic analysis of the failed samples, SLM series demonstrated a predominantly transgranular failure features and a global ductile behavior; whereas CS samples maintained the brittle matrix while recovering some ductility represented by the areas covered by dimples. Density of the dimples was enhanced by increasing the applied temperature, as the CS-HTB series represented a more ductile behavior compared to the CS-HTA ones. The features observed on fracture surfaces correlate well with the static tensile test results. Various defects were identified on the fracture surface of SLM-HTC series. The presence of such defects could have been responsible for the limited ductility as well as high scatter in the fatigue test data obtained for this series. The more uniform distribution of grain size in SLM-HTC samples after recrystallization could have contributed to the higher UTS obtained for this series compared to all the other SLM series.

5. Conclusions

Freestanding high density cold spray deposited Inconel 718 samples were compared before and after various heat treatments with those fabricated by selective laser melting. Cold spray resulted in a homogeneous structure and preserved the original microstructure of the feedstock powder, which can be a notable advantage with respect to the selective laser melting series. Heat treatments promoted inter-particle metallurgical bonding and resulted in remarkable cohesive strength and ductility enhancement of cold sprayed series. First time study of fatigue strength of both cold spray and selective laser melting deposited Inconel 718 samples, indicated outstanding room temperature fatigue strength corresponding to 2 million cycles that was found to be comparable to that of wrought and cast bulk material for both tested series.

Besides comparable mechanical properties and noteworthy fatigue strength, cold spray has the high potential to address some of the shortcomings of the commonly used additive manufacturing techniques including high working temperature, size limitations and much lower deposition rate. Since cold spray is able to induce a notable surface work hardening with associated higher hardness and lower ductility, the application of the optimal heat treatment able to increase the

ductility of the cold spray deposited material is a key factor. In addition, there are still some limits hindering commercialization of cold spray as an additive manufacturing technique, including geometrical accuracy. Nevertheless, the results of this study bring light on the extraordinary potential of high quality freestanding cold spray deposited material with notable structural integrity to be used as load bearing components at a wide range of prospective applications. The presented data encourage further investigation for addressing the present technological limits.

Acknowledgements

The authors declare no conflict of interests in this work. SB, MVZ and MG acknowledge financial support from ECOFRONT project defined in the framework of Alta Scuola Politecnica (ASP).

Appendix A. Supplementary material

Supplementary data associated with this article can be found in the online version at <http://dx.doi.org/10.1016/j.msea.2018.02.094>.

References

- [1] R. Ghelichi, S. Bagherifard, M. Guagliano, M. Verani, Numerical simulation of cold spray coating, *Surf. Coat. Technol.* 205 (2011) 5294–5301.
- [2] R. Ghelichi, M. Guagliano, Coating by the cold spray process: a state of the art, *Fract. Struct. Integr.* (2009) 30–44.
- [3] V. Champagne, D. Helfrich, The unique abilities of cold spray deposition, *Int. Mater. Rev.* 61 (2016) 437–455.
- [4] V.K. Champagne, *The Cold Spray Materials Deposition Process: Fundamentals and Applications*, Woodhead Publishing, 2007 eBook ISBN: 9781845693787.
- [5] R. Ghelichi, S. Bagherifard, D. MacDonald, M. Brochu, H. Jahed, B. Jodoin, et al., Fatigue strength of Al alloy cold sprayed with nanocrystalline powders, *Int. J. Fatigue* 65 (2014) 51–57.
- [6] A.W.-Y. Tan, S. Wen, N.W. Khun, I. Marinescu, Z. Dong, E. Liu, Potential of Cold Spray as Additive Manufacturing for Ti6Al4V, 2016.
- [7] H. Attar, S. Ehtemam-Haghighi, D. Kent, X. Wu, M.S. Dargusch, Comparative study of commercially pure titanium produced by laser engineered net shaping, selective laser melting and casting processes, *Mater. Sci. Eng.: A* 705 (2017) 385–393.
- [8] H. Attar, M. Bönnisch, M. Calin, L.-C. Zhang, S. Scudino, J. Eckert, Selective laser melting of in situ titanium–titanium boride composites: processing, microstructure and mechanical properties, *Acta Mater.* 76 (2014) 13–22.
- [9] S. Scudino, C. Unterdörfer, K. Prashanth, H. Attar, N. Ellendt, V. Uhlenwinkel, et al., Additive manufacturing of Cu–10Sn bronze, *Mater. Lett.* 156 (2015) 202–204.
- [10] K.G. Prashanth, H. Shakur Shahabi, H. Attar, V.C. Srivastava, N. Ellendt, V. Uhlenwinkel, et al., Production of high strength Al85Nd8Ni5Co2 alloy by selective laser melting, *Addit. Manuf.* 6 (2015) 1–5.
- [11] M.E. Lynch, W. Gu, T. El-Wardany, A. Hsu, D. Viens, A. Nardi, et al., Design and topology/shape structural optimisation for additively manufactured cold sprayed components: this paper presents an additive manufactured cold spray component which is shape optimised to achieve 60% reduction in stress and 20% reduction in weight, *Virtual Phys. Prototyp.* 8 (2013) 213–231.
- [12] A. Sova, S. Grigoriev, A. Okunkova, I. Smurov, Potential of cold gas dynamic spray as additive manufacturing technology, *Int. J. Adv. Manuf. Technol.* 69 (2013) 2269–2278.
- [13] V. Champagne, D. Helfrich, E. Wienhold, J. DeHaven, The development of nickel–aluminum reactive material by cold spray process, *Army Res. Lab. Tech. Rep. ARL-TR 5189* (2010).
- [14] Y. Cormier, P. Dupuis, B. Jodoin, A. Corbeil, Net shape fins for compact heat exchanger produced by cold spray, *J. Therm. Spray Technol.* 22 (2013) 1210–1221.
- [15] R.H. Morgan, C.J. Sutcliffe, J. Pattison, M. Murphy, C. Gallagher, A. Papworth, et al., Cold gas dynamic manufacturing – a new approach to near-net shape metal component fabrication, *MRS Proc.* (2002) 758.
- [16] P. Vo MM, Layer-by-layer buildup strategy for cold spray additive manufacturing, in: *Proceedings of the International Thermal Spray Conference and Exposition (ITSC)*, Düsseldorf, Germany, 2017, pp. 714–718.
- [17] S. Cadney, M. Brochu, P. Richer, B. Jodoin, Cold gas dynamic spraying as a method for freeforming and joining materials, *Surf. Coat. Technol.* 202 (2008) 2801–2806.
- [18] D. MacDonald, R. Fernández, F. Delloro, B. Jodoin, Cold spraying of Armstrong process titanium powder for additive manufacturing, *J. Therm. Spray Technol.* (2016) 1–12.
- [19] A. Thomas, M. El-Wahabi, J. Cabrera, J. Prado, High temperature deformation of Inconel 718, *J. Mater. Process. Technol.* 177 (2006) 469–472.
- [20] M. Sundararaman, P. Mukhopadhyay, S. Banerjee, Precipitation of the δ -Ni₃Nb phase in two nickel base superalloys, *Metall. Trans. A* 19 (1988) 453–465.
- [21] Y. Wang, J. Shi, S. Lu, Y. Wang, Selective laser melting of graphene-reinforced Inconel 718 superalloy: evaluation of microstructure and tensile performance, *J. Manuf. Sci. Eng.* 139 (2017) 041005.
- [22] F. Liu, X. Lin, C. Huang, M. Song, G. Yang, J. Chen, et al., The effect of laser

- scanning path on microstructures and mechanical properties of laser solid formed nickel-base superalloy Inconel 718, *J. Alloy. Compd.* 509 (2011) 4505–4509.
- [23] L.L. Parimi, G. Ravi, D. Clark, M.M. Attallah, Microstructural and texture development in direct laser fabricated IN718, *Mater. Charact.* 89 (2014) 102–111.
- [24] E. Chlebus, K. Gruber, B. Kuźnicka, J. Kurzac, T. Kurzynowski, Effect of heat treatment on the microstructure and mechanical properties of Inconel 718 processed by selective laser melting, *Mater. Sci. Eng.: A* 639 (2015) 647–655.
- [25] Y. Lu, S. Wu, Y. Gan, T. Huang, C. Yang, L. Junjie, et al., Study on the microstructure, mechanical property and residual stress of SLM Inconel-718 alloy manufactured by differing island scanning strategy, *Opt. Laser Technol.* 75 (2015) 197–206.
- [26] Q. Jia, D. Gu, Selective laser melting additive manufacturing of Inconel 718 superalloy parts: densification, microstructure and properties, *J. Alloy. Compd.* 585 (2014) 713–721.
- [27] D. Zhang, W. Niu, X. Cao, Z. Liu, Effect of standard heat treatment on the microstructure and mechanical properties of selective laser melting manufactured Inconel 718 superalloy, *Mater. Sci. Eng.: A* 644 (2015) 32–40.
- [28] K. Amato, S. Gaytan, L. Murr, E. Martinez, P. Shindo, J. Hernandez, et al., Microstructures and mechanical behavior of Inconel 718 fabricated by selective laser melting, *Acta Mater.* 60 (2012) 2229–2239.
- [29] A. Spierings, T. Starr, K. Wegener, Fatigue performance of additive manufactured metallic parts, *Rapid Prototyp. J.* 19 (2013) 88–94.
- [30] A. Riemer, S. Leuders, M. Thöne, H. Richard, T. Tröster, T. Niendorf, On the fatigue crack growth behavior in 316L stainless steel manufactured by selective laser melting, *Eng. Fract. Mech.* 120 (2014) 15–25.
- [31] E. Brandl, U. Heckenberger, V. Holzinger, D. Buchbinder, Additive manufactured AISi10Mg samples using selective laser melting (SLM): microstructure, high cycle fatigue, and fracture behavior, *Mater. Des.* 34 (2012) 159–169.
- [32] S. Leuders, M. Thöne, A. Riemer, T. Niendorf, T. Tröster, H. Richard, et al., On the mechanical behaviour of titanium alloy TiAl6V4 manufactured by selective laser melting: fatigue resistance and crack growth performance, *Int. J. Fatigue* 48 (2013) 300–307.
- [33] P. Kanagarajah, F. Brenne, T. Niendorf, H.J. Maier, Inconel 939 processed by selective laser melting: effect of microstructure and temperature on the mechanical properties under static and cyclic loading, *Mater. Sci. Eng.: A* 588 (2013) 188–195.
- [34] T. Marrocco, D. McCartney, P. Shipway, A. Sturgeon, Comparison of the Microstructure of Cold Sprayed and Thermally Sprayed IN718 Coatings, May 2006, pp. 15–18.
- [35] W. Wong, E. Irissou, P. Vo, M. Sone, F. Bernier, J.-G. Legoux, et al., Cold spray forming of Inconel 718, *J. Therm. Spray Technol.* 22 (2013) 413–421.
- [36] D. Levasseur, S. Yue, M. Brochu, Pressureless sintering of cold sprayed Inconel 718 deposit, *Mater. Sci. Eng.: A* 556 (2012) 343–350.
- [37] R. Singh, K.-H. Rauwald, E. Wessel, G. Mauer, S. Schrufer, A. Barth, et al., Effects of substrate roughness and spray-angle on deposition behavior of cold-sprayed Inconel 718, *Surf. Coat. Technol.* (2017).
- [38] S. Bagherifard, G. Roscioli, M.V. Zuccoli, M. Hadi, G. D'Elia, A.G. Demir, et al., Cold spray deposition of freestanding inconel samples and comparative analysis with selective laser melting, *J. Therm. Spray Technol.* (2017) 1–10.
- [39] AMS5662, Nickel Alloy, Corrosion and Heat-Resistant, Bars, Forgings, and Rings, Aerospace Material Specification, SAE International Group, 2004.
- [40] C.A. Schneider, W.S. Rasband, K.W. Eliceiri, NIH Image to ImageJ: 25 years of Image analysis, *Nat. Methods* 9 (2012) 671–675.
- [41] W.J. Dixon, F.J. Massey, Introduction to Statistical Analysis, McGraw-Hill, New York, 1969.
- [42] K. Brownlee, J. Hodges Jr, M. Rosenblatt, The up-and-down method with small samples, *J. Am. Stat. Assoc.* 48 (1953) 262–277.
- [43] W. Liu, M. Yao, Z. Chen, S. Wang, Niobium segregation in Inconel 718, *J. Mater. Sci.* 34 (1999) 2583–2586.
- [44] H.-S. Park, J. Park, Precipitation in Inconel 718 alloy, *Nucl. Eng. Technol.* 4 (1972) 203–213.
- [45] W.C. Liu, M. Yao, Z.L. Chen, S.G. Wang, Niobium segregation in Inconel 718, *J. Mater. Sci.* 34 (1999) 2583–2586.
- [46] Inconel Alloy 718 Properties. <<http://www.specialmetals.com>> ed: Special Metals, 2017.
- [47] R. Huang, H. Fukunum, Study of the properties of cold-sprayed In718 deposits, in: Proceedings of the International Thermal Spray Conference, Shanghai, China, 2016, pp. 299–304.
- [48] Total Materia The World's Most Comprehensive Materials Database: Key to Metals AG 2016.
- [49] P. Jindal, A. Santhanam, U. Schleinkofer, A. Shuster, Performance of PVD TiN, TiCN, and TiAlN coated cemented carbide tools in turning, *Int. J. Refract. Met. Hard Mater.* 17 (1999) 163–170.
- [50] J. Hong, J. Park, N. Park, I. Eom, M. Kim, C. Kang, Microstructures and mechanical properties of Inconel 718 welds by CO₂ laser welding, *J. Mater. Process. Technol.* 201 (2008) 515–520.
- [51] Q. Chen, N. Kawagoishi, H. Nisitani, Evaluation of fatigue crack growth rate and life prediction of Inconel 718 at room and elevated temperatures, *Mater. Sci. Eng.: A* 277 (2000) 250–257.
- [52] X.-f. Ma, Z. Duan, H.-j. Shi, R. Murai, E. Yanagisawa, Fatigue and fracture behavior of nickel-based superalloy Inconel 718 up to the very high cycle regime, *J. Zhejiang Univ.-Sci.* A 11 (2010) 727–737.
- [53] SpecialMetals Specifications for INCONEL® Alloy 718 (UNS N07718/W.Nr. 2.4668) <www.specialmetals.com> 1-28.
- [54] S. Suresh, Fatigue of Materials, Cambridge University Press, Cambridge, 1998 ISBN 0-521-43763-6.
- [55] G. Marchese, X. Garmendia Colera, F. Calignano, M. Lorusso, S. Biamino, P. Minetola, et al., Characterization and comparison of Inconel 625 processed by selective laser melting and laser metal deposition, *Adv. Eng. Mater.* (2016).
- [56] A. Chaudhuri, Y. Raghupathy, D. Srinivasan, S. Suwas, C. Srivastava, Microstructural evolution of cold-sprayed Inconel 625 superalloy coatings on low alloy steel substrate, *Acta Mater.* (2017).
- [57] F. Liu, X. Lin, G. Yang, M. Song, J. Chen, W. Huang, Microstructure and residual stress of laser rapid formed Inconel 718 nickel-base superalloy, *Opt. Laser Technol.* 43 (2011) 208–213.
- [58] R. Giusti, S. Vezzù, G. Lucchetta, Wear-resistant cobalt-based coatings for injection moulds by cold spray, *Surf. Eng.* 32 (2016) 677–685.
- [59] R. Ghelichi, S. Bagherifard, D. MacDonald, I. Fernandez-Pariente, B. Jodoin, M. Guagliano, Experimental and numerical study of residual stress evolution in cold spray coating, *Appl. Surf. Sci.* 288 (2014) 26–33.
- [60] R. Ghelichi, D. MacDonald, S. Bagherifard, H. Jahed, M. Guagliano, B. Jodoin, Microstructure and fatigue behavior of cold spray coated Al5052, *Acta Materialia* 60 (19) (2012) 6555–6561.